

# MHD modelling of open flux evolution around solar maximum by coronal model COCONUT

H. P. Wang<sup>1</sup>, S. Poedts<sup>1,2</sup>, A. Lani<sup>1,3</sup>, L. Linan<sup>1</sup>, T. Baratashvili<sup>1</sup>, H.-J. Jeong<sup>1,4</sup>, R. Dhib<sup>1</sup>, Q. Noraz<sup>1</sup>, W. W. Wei<sup>5</sup>, M. Najafi-Ziyazi<sup>1</sup>, J. Y. Liu<sup>1</sup>, H. Wu<sup>1</sup>, R. Zhuo<sup>1</sup>, J. Murteira<sup>1</sup>, K. Arabuli<sup>1</sup>, B. Schmieder<sup>1,6,7</sup>, and J. Magdalenic<sup>1,8</sup>

<sup>1</sup> Centre for Mathematical Plasma-Astrophysics, Department of Mathematics, KU Leuven, Celestijnenlaan 200B, 3001 Leuven, Belgium

e-mail: Stefaan.Poedts@kuleuven.be

e-mail: andrea.lani@kuleuven.be

e-mail: haopeng.wang1@kuleuven.be

<sup>2</sup> Institute of Physics, University of Maria Curie-Skłodowska, ul. Radziszewskiego 10, 20-031 Lublin, Poland

<sup>3</sup> Von Karman Institute For Fluid Dynamics, Waterlosesteenweg 72, 1640 Sint-Genesius-Rode, Brussels, Belgium

<sup>4</sup> School of Space Research, Kyung Hee University, Yongin, 17104, Republic of Korea

<sup>5</sup> Space Sciences Laboratory, University of California, Berkeley, CA 94720, USA

<sup>6</sup> Observatoire de Paris, LIRA, UMR8254 (CNRS), F-92195 Meudon Principal Cedex, France

<sup>7</sup> LUNEX EMMESI COSPAR-PEX Eurospacehub, Kapteyn straat 1, Noordwijk 2201 BB, Netherlands

<sup>8</sup> Solar-Terrestrial Centre of Excellence—S IDC, Royal Observatory of Belgium, 1180 Brussels, Belgium

January 16, 2026

## ABSTRACT

**Context.** Recently, the numerical stability of the time-evolving coronal magnetohydrodynamic (MHD) model COCONUT has been significantly improved by the energy decomposition strategy that effectively addresses low- $\beta$  issues. This provides an opportunity to explore the “open flux problem” through time-evolving coronal MHD simulations during solar maximum without significant simplifications.

**Aims.** In this paper, we perform time-evolving MHD coronal simulations for two solar maximum Carrington rotations (CRs) to investigate the evolution of open magnetic flux at different heliocentric distances. We also examine the effects of magnetogram preprocessing using a limited set of spherical harmonics and of empirically defined heating source terms on the simulated coronal evolution.

**Methods.** In coronal MHD simulations, the commonly used magnetogram preprocessing using a potential field (PF) solver with limited spherical harmonics can overly smooth out small-scale magnetic structures and alter the open-field distributions. The evolution of the magnetic field at the solar surface and the empirically defined heating source terms can also affect the open-field distributions. To evaluate these factors, we use a series of hourly-updated magnetograms, preprocessed by the 10th- and 50th-order filtered PF solvers, to drive COCONUT, configured with different heating prescriptions, to mimic coronal evolutions during CRs 2282 and 2283. We evaluate the simulated open magnetic flux at  $1.01 R_s$ ,  $3 R_s$ , and  $0.1$  AU, and compare them with interplanetary observations.

**Results.** The results show that the simulated unsigned open flux evaluated near the solar surface can be comparable to that derived from interplanetary *in situ* observations. However, in low corona, numerous small-scale closed-field magnetic structures introduce magnetic polarity inversion interfaces within the open field, cancelling part of the open field near these interfaces during the volume-integration procedure of the finite-volume method. Consequently, the simulated unsigned open flux can be reduced by up to 45% at  $0.1$  AU and decreases more rapidly in the low corona. The results also indicate that moderate adjustments to the heating source term can effectively regulate the magnitude of the unsigned open magnetic flux. Preprocessing the initial magnetogram by a PF solver with limited spherical harmonics can reduce the open flux in the low corona and alter the distribution of open-field regions, but has little effect on the total unsigned open flux at larger heliocentric distances. Additionally, the ratio of the maximum to minimum open unsigned magnetic flux can reach 1.4 within a single solar maximum CR. These findings highlight the necessity of considering finer grid resolution around magnetic polarity inversion interfaces, more realistic heating mechanisms, and the time-evolving regime of MHD coronal modelling when further addressing the “open flux problem”.

**Key words.** Sun: magnetohydrodynamics (MHD) –methods: numerical –Sun: corona

## 1. Introduction

Most of the magnetic flux threading the photosphere returns to the solar surface, forming closed magnetic field lines in the corona, whereas the open magnetic field extends into interplanetary space, linking the Sun and Earth and forming the interplanetary magnetic field. These open fields drive geomagnetic activity that affects daily life, guide the propagation of solar energetic particles, and help shield the solar system from galactic

cosmic rays (e.g. Schrijver & De Rosa 2003; Erdős & Balogh 2012; Linker et al. 2017; Frost et al. 2022). Additionally, the relationship between long-term variations in solar open magnetic flux, solar activity, and potentially climate change remains an active area of investigation. (Erdős & Balogh 2012). It is important to understand the mechanisms driving the evolution of the open magnetic flux.

It is widely accepted that coronal holes (CHs), characterised by rapidly expanding open field lines and appearing dark in ex-

treme ultraviolet (EUV) and X-ray images (Linker et al. 1999; Cranmer 2002; Feng et al. 2015, 2017, 2019), are the primary sources of open magnetic flux. However, it was noted that the magnetic flux derived from observation-based CH regions in synoptic line-of-sight photospheric magnetograms is smaller than that measured *in-situ* in interplanetary space. Moreover, the open magnetic flux, extrapolated numerically from the observed magnetograms into interplanetary space, is typically underestimated by a factor of two or more. This discrepancy is widely known as the “open flux problem”, a well-known challenge in coronal modelling (Linker et al. 2017). It has been proposed that magnetic maps derived from observations may underestimate the total magnetic flux (e.g. Sinjan et al. 2024) or that a substantial fraction of the open magnetic flux originates from regions that do not appear dark in emission (Linker et al. 2017; Linker et al. 2021).

The open magnetic flux can be evaluated by directly measuring the magnetic flux density using magnetometers onboard space probes. *Ulysses* (Wenzel et al. 1992; Smith & Balogh 1995) observations indicated that the magnetic flux density remains nearly uniform with the heliographic latitude at a given heliocentric distance (except near the heliospheric current sheet; Balogh et al. 1995; Smith & Balogh 1995; Lockwood et al. 2004). Owens et al. (2008) further validated this finding using estimates of the total heliospheric magnetic flux obtained from widely separated spacecraft, and revealed a tendency for the estimated flux to increase with heliocentric distance, which may be caused by inversions of heliospheric magnetic field lines (Erdős & Balogh 2012; Erdős & Balogh 2014; Lockwood et al. 2009; Owens et al. 2017; Frost et al. 2022). This variation mainly arises from magnetic field fluctuations around the Parker spiral structure (Erdős & Balogh 2012), due to  $B_r$ , decreases with the heliospheric distance faster than the fluctuation amplitude (Smith 2011). It was also reported that the warped current sheet, along with transient events such as corotating interaction regions and CMEs, can induce tilts in the heliospheric magnetic field, thereby contributing to the measured excess flux (Lockwood 2002).

By adopting the supra-thermal electron beam method to distinguish between different heliospheric magnetic field topologies, it was found that magnetic field line inversions account for approximately 20% of the measured magnetic flux in ACE data (McComas et al. 1998; Smith et al. 1998; King & Papiashvili 2005) collected during 1998-2011 (Owens et al. 2017). Kinematic corrections based on the observed solar wind velocity structure have been proposed to mitigate the influence of large-scale spatial velocity gradients on open flux estimates (Lockwood et al. 2009). The *in-situ* electron and magnetic field data is also used to determine the global topology of the heliospheric magnetic field and identify field line inversions. With the development of these technologies, it has been demonstrated that the best heliospheric estimate of open flux remains, on average, a factor of 1.6 higher than the values extrapolated from photospheric observations (Frost et al. 2022).

By measuring the magnetic field observed by the FIELDS instrument (Bale et al. 2016) onboard the Parker Solar Probe (PSP; Fox et al. 2016) along the Parker spiral, and then projecting it radially to correct for excess flux caused by field line inversions (Erdős & Balogh 2012; Erdős & Balogh 2014), it was found that the total unsigned *in-situ* magnetic flux remains nearly constant between 0.13 AU and 0.8 AU (Badman, Samuel T. et al. 2021). From MHD simulations, Riley et al. (2021) showed that the underestimated magnetic flux persists even down to 26.9  $R_s$ . Additionally, it was reported that the magnetic field may continue

to vary along the latitude out to at least 10  $R_s$  (Réville & Brun 2017), highlighting the necessity of modelling the evolution of open flux down to the trans-Alfvénic region in order to assess how magnetic flux evolves with heliospheric distance.

Using CH detections, the open magnetic flux can be estimated by integrating the magnetic flux within the CH regions identified on photospheric magnetograms. However, open magnetic flux is also present outside CHs and transported across the solar surface via interchange reconnection with closed magnetic loops (Fisk 2005; Iijima 2025). The complex structure and dynamic interactions between closed and open magnetic fields near the CH boundary introduce uncertainties in CH detection. Even when advanced CH detection techniques are applied to MHD simulation results, there remains a tendency to overestimate the open-flux area. However, it underestimated the total simulated open magnetic flux by  $\sim 30\text{-}40\%$  (Linker et al. 2021), still insufficient to account for the observed missing flux.

The magnetograph measurements may also lead to the missed open flux. The Zeeman-Doppler imaging (ZDI) magnetograms of stellar surface magnetic fields suffer from missing information in regions obscured by dark starspots or hidden from view due to the rotation axis’ inclination (Jardine et al. 2010; Johnstone et al. 2010). The magnetic field that ZDI fails to recover in these regions, or misses due to limited spatial resolution, may lead to an underestimation of the open magnetic flux. By analysing simulated solar photospheric magnetic fields, Milić et al. (2024) and Sinjan, J. et al. (2024) showed that reduced telescope resolution leads to a lower estimated mean magnetic flux density, and recommended using high-resolution observations when performing magnetic field extrapolations to reduce the effect of the underestimated unipolar magnetic flux. Additionally, Wang et al. (2022) showed that by applying saturation corrections (e.g., Ulrich et al. 2009) to MWO and WSO photospheric magnetograms, and then extrapolating the magnetic field from them with the PFSS model, the derived open flux can be consistent with the observed interplanetary magnetic flux. Wang et al. (2025a) showed that inserting an observation-derived flux-rope field into the inner-boundary magnetic field leads to a larger open-field region that is more consistent with CH observations.

There are also simulation research works related to the “open flux problem”. Potential field source surface (PFSS) simulations indicated that the total nondipole flux component is at least an order of magnitude larger than the dipole flux (Yoshida et al. 2023). Riley et al. (2019) added additional polar flux to photospheric magnetograms to (partially) resolve the “open flux problem” in PFSS and MHD simulations during solar minimum. Wallace et al. (2019) showed that the total open flux derived from observed CHs agrees well with the semi-empirical Wang-Sheeley-Arge (WSA) simulation results (Wang & Sheeley 1990; Arge et al. 2004), and both deviated from the *in-situ* observations, especially near solar maximum. Arge et al. (2024) showed that adjusting the boundary by about one supergranular width, a key scale in open-closed flux dynamics (Aslanyan et al. 2022), is sufficient to align the modelled open flux in the WSA simulations with *in situ* observations. Caplan et al. (2021) found that increasing the grid resolution in PF simulations reduces open-field areas, increases the unsigned magnetic flux, and hardly impacts the net open flux, and showed that the choice of source surface radius strongly influences the calculated open flux. Wang et al. (2025e) indicated that increasing the tangential grid resolution by  $4 \times 4$  times (from  $\sim 3.6^\circ$  to  $\sim 0.9^\circ$ ) in MHD coronal simulation led to an increase of  $\sim 40\%$  in the average magnetic field strength. Besides, Asvestari et al. (2024) showed that the MHD model produces significantly more open flux than the PF models.

Moreover, Yeates et al. (2010) and Mackay & Upton (2022) inserted magnetic dipoles, determined from observational synoptic magnetograms, into their coronal simulations to provide a continuously evolving boundary condition for the non-potential magnetofrictional model. It is observed that surface motions drive the twisted magnetic flux ropes to erupt and induce fluctuations in the open magnetic flux. High-cadence bipole data derived from hourly updated advective flux transport (AFT) magnetograms (Upton & Hathaway 2014) produced more open flux than the 27-day Carrington-rotation maps, and non-potential simulations yield substantially higher open flux than PFSS models (Mackay & Upton 2022). Considering that MF models cannot capture the dynamic features of the plasma, corresponding time-evolving MHD coronal simulations are required to investigate magnetic flux evolutions in a more self-consistent manner. Consequently, coronal MHD models that can simultaneously achieve high computational efficiency, strong numerical stability, and high spatial and temporal resolution are required to perform such simulations.

In general, MHD models of the solar corona and wind can be classified into two categories: quasi-steady models and time-evolving models. Models constrained by a single static magnetogram (e.g. Perri et al. 2018, 2022, 2023; Mikić et al. 2018; Wang et al. 2019; Feng et al. 2005, 2010, 2021; Parenti et al. 2022; Kužma et al. 2023; Linan et al. 2023; Liu et al. 2023; Wang et al. 2022a,b, 2025a,b; Brchneva et al. 2023) are referred to as quasi-steady-state models, whereas those driven by a sequence of time-evolving magnetograms (e.g. Yang et al. 2012; Hayashi et al. 2021; Hoeksema et al. 2020; Feng et al. 2023; Lionello et al. 2023; Mason et al. 2023; Wang et al. 2025c,e,f) are defined as time-evolving models. The former assume a (quasi-)steady corona over one CR, whereas the latter are time-accurate and driven by continuously updated magnetograms, thereby enabling a more realistic representation of the evolving solar coronal and wind structures. A more detailed description of these two coronal modelling regimes is available in Wang et al. (2025c,e,f).

Currently, implicit temporal integration methods, which allow selecting larger time steps than the explicit method, have significantly improved the computational efficiency of quasi-steady-state coronal MHD models (Perri et al. 2022, 2023; Wang et al. 2019; Feng et al. 2021; Wang et al. 2022a,b), achieving tens to hundreds of speed-ups compared to explicit models. Moreover, the time-evolving coronal MHD models COOlfluid COOrOal UnsTructured (COCONUT) (COCONUT; Wang et al. 2025c,d,e) and Solar Interplanetary Phenomena Implicit Finite Volume Method (SIP-IFVM) (SIP-IFVM; Wang et al. 2025f), both adopting implicit methods, realise faster-than-real-time simulations by only about twenty CPUs, with grid resolutions of 1.5 million (M) and 1 M cells and time steps of 10 and 3-4 minutes, respectively. Whereas the commonly used explicit or semi-implicit time-evolving coronal MHD models (Hoeksema et al. 2020; Downs et al. 2025) typically require thousands of CPUs to achieve comparable performance. Moreover, the extended magnetic field decomposition method (Wang et al. 2025f) and the decomposed energy strategy combined with an Harten-Lax-van Leer (HLL) Riemann solver with an additional dissipation term in the energy equation (Wang et al. 2025d) enable SIP-IFVM and COCONUT, respectively, to perform time-evolving MHD coronal simulations involving low- $\beta$  (thermal-to-magnetic pressure ratio) issues (Feng et al. 2021; Wang et al. 2022a, 2025d,f).

In this paper, we use the time-evolving COCONUT, a novel implicit coronal model built on the Computational Object-Oriented Libraries for Fluid Dynamics (COOLFluiD) frame-

work (Kimpe et al. 2005; Lani et al. 2005, 2013)<sup>1</sup>, to simulate the evolution of open flux during two solar-maximum CRs, as a preparation for a comprehensive whole-solar-cycle MHD simulation of open flux evolution in the future. Inherent from high efficiency, COCONUT (Wang et al. 2025c,e) has finished a continuously evolving coronal simulation dataset that covers three years around the solar minimum to train the machine-learning neural network (Li et al. 2025). To achieve the required numerical stability, the previous COCONUT adopted positivity-preserving (PP) measures for density and pressure. Additionally, commonly used preprocessing procedures, such as spherical harmonic filtering on photospheric magnetograms (Kužma et al. 2023; Wang et al. 2025e), may also affect simulation results. Given that the numerical stability of COCONUT has been significantly improved by the decomposed-energy strategy (Wang et al. 2025d), we further investigate the impact of these numerical measures on the simulation results.

Based on the above considerations, the paper is organised as follows. In Section 2, we describe the numerical setup of COCONUT used in this study, including the PP measures, the heating terms, the radiative cooling terms, the thermal conduction terms and various input data. In Section 3, we present the evolution of the open magnetic flux, the distributions of open-field regions, and the 2D timing diagrams of plasma parameters during solar maximum CRs 2282 and 2283 simulated by COCONUT. Simulation results with different model setups are compared to assess uncertainties in coronal MHD modelling. Comparisons with white-light coronal observations and interplanetary *in situ* observations are also provided. In Section 4, we summarise the magnetic flux evolution driven by different preprocessed magnetograms, analyse the impact of modelling uncertainties in MHD coronal simulations, and provide concluding remarks.

## 2. Numerical setup in COCONUT

In this paper, we use the coronal MHD model COCONUT, which employs the decomposed energy strategy and the HLL Riemann solver with an additional dissipation term added to the energy equation to improve numerical stability in addressing low- $\beta$  issues (Wang et al. 2025d), to simulate coronal evolutions during two solar maximum CR. The impact of several numerical modifications introduced in Wang et al. (2025c,e), originally developed to improve numerical stability, is also evaluated using this version of COCONUT.

### 2.1. The governing equations and grid system

A spherical-shell computational domain extending from 1.01 to  $\sim 25 R_s$ , discretised into about 1.5 million (M) truncated pentagonal-pyramid cells (Brchneva et al. 2022), with a tangential angular resolution of approximately 1.8° (Wang et al. 2025c,e), is adopted for the simulations. The governing equations are the same as those in (Wang et al. 2025d) and can be described in the following form:

$$\frac{\partial \mathbf{U}}{\partial t} + \nabla \cdot \mathbf{F}(\mathbf{U}) = \mathbf{S}(\mathbf{U}, \nabla \mathbf{U}),$$

where  $t$  and  $\mathbf{U}$  refer to the time and vector of conservative variables,  $\nabla \mathbf{U}$  means the spatial derivative of  $\mathbf{U}$ , and  $\mathbf{F}(\mathbf{U})$  is the inviscid flux vector,  $\mathbf{S}(\mathbf{U}, \nabla \mathbf{U}) = \mathbf{S}_{\text{gra}} + \mathbf{S}_{\text{heat}} + \mathbf{S}_{\text{DECOMP}}$  denotes the vector of the source terms corresponding to the

<sup>1</sup> <https://github.com/andrealani/COOLFluiD/wiki>

gravitational force, the heating source terms, and the source term derived from the decomposed energy equation described in Wang et al. (2025d). We calculate  $\mathbf{S}_{\text{gra}}$  and  $\mathbf{S}_{\text{DECOMP}}$  in the same way as before, but vary the calculation of  $\mathbf{S}_{\text{heat}}$  to evaluate its impact on global coronal MHD modelling. The term  $\mathbf{S}_{\text{heat}} = -\nabla \cdot \mathbf{q} + Q_{\text{rad}} + Q_H$  consists of optically thin radiative loss  $Q_{\text{rad}}$ , empirically defined coronal heating  $Q_H$ , and Spitzer or collisionless thermal conduction term  $-\nabla \cdot \mathbf{q}$ .

As usual,  $Q_{\text{rad}}$  is calculated the same as in Wang et al. (2025c,e). The thermal conduction term is computed following the approach described in Baratashvili et al. (2024) and Wang et al. (2025c). As usual,  $Q_H$  can be calculated by the following formulation (Mok et al. 2005; Downs et al. 2010; Baratashvili et al. 2024; Wang et al. 2025b,e):

$$Q_H = H_0 \cdot |\mathbf{B}| \cdot e^{-\frac{r-R_s}{\lambda}}, \text{ with } H_0 = 4 \cdot 10^{-2} \text{ J m}^{-3} \text{ s}^{-1} \text{ T}^{-1}, \quad (1)$$

where  $\mathbf{B}$  is the magnetic field vector, and  $\lambda = 0.7 R_s$ . To evaluate the uncertainty associated with the empirically defined  $Q_H$ , we also tested the following slightly modified form for comparison:

$$Q_H = H_0 \cdot |\mathbf{B}| \cdot \frac{r}{R_s} \cdot e^{-\frac{r-R_s}{\lambda}}, \text{ with } H_0 = 2 \cdot 10^{-2} \text{ J m}^{-3} \text{ s}^{-1} \text{ T}^{-1}. \quad (2)$$

Inspired by the empirically defined volumetric heating source terms (e.g., Nakamizo et al. 2009; Feng et al. 2010, 2021; Wang et al. 2022a), which introduce a dimensionless heliocentric distance parameter into the exponentially decaying term, we further scale Eq. (1) by  $\frac{r}{R_s}$  to obtain Eq. (2). Because  $\frac{r}{R_s} \geq 1$ , multiplying the heating term by this factor increases the prescribed heating. To avoid introducing an unrealistically large energy input, we reduce  $H_0$  in Eq. (2) so that the overall heating remains comparable to the original formulation. This comparison is not intended to identify a superior empirical heating source term, but rather to assess how radial variations in heating prescriptions alter the simulated coronal structures.

## 2.2. Inner boundary setups

A series of hourly update photospheric magnetograms is used to drive coronal evolutions. These simulations are conducted in a heliocentric inertial coordinate system (Burlaga 1984; Fränz & Harper 2002) with the Earth permanently positioned at  $\phi = 60^\circ$ . During the time-evolving coronal simulations, the inner-boundary radial magnetic field at each physical time step is interpolated from four adjacent observation-based magnetograms using cubic Hermite interpolation (Wang et al. 2025c).

Since the chromosphere and transition region are not included in our model, the inner-boundary radial magnetic field  $B_{r,s}$  is defined by employing a PF solver with the high-order spherical harmonic components removed to extrapolate the photospheric magnetograms to the base of the low corona. To evaluate the impact of this preprocessing, which smooths out small-scale magnetic structures, we adopt two sets of magnetograms to drive coronal evolutions.

1. We use a 10th-order spherical-harmonic PF solver, in which the spherical-harmonic expansion of the scalar potential  $\mathcal{U}$  is given by

$$\mathcal{U} \approx \sum_{l=1}^{10} \sum_{m=-l}^l I_l^m Y_l^m(\mu, \phi). \quad (3)$$

2. We employ a 50th-order spherical-harmonic PF solver with a filter (McClarren & Hauck 2010; Wang et al. 2025e;

**Table 1.** Numerical setup of the time-evolving coronal simulations.

Case	heating source term	inner boundary magnetic field
1	Eq. (1)	Eq. (3)
2	Eq. (1)	Eq. (4)
3	Eq. (2)	Eq. (4)

Murteira et al. 2025), expressed as

$$\mathcal{U}_{\text{filtered}} \approx \sum_{l=1}^{50} \sum_{m=-l}^l \frac{I_l^m Y_l^m(\mu, \phi)}{1 + \xi l^2(l+1)^2}, \text{ with } \xi = 3 \times 10^{-6}. \quad (4)$$

In Eqs. (3) and (4),  $Y_l^m$  and  $I_l^m$  denote the spherical harmonic function and corresponding spectral coefficient of degree  $l$  and order  $m$ ,  $\mu \equiv \cos \theta$ ,  $\theta \in [0, \pi]$  and  $\phi \in [0, 2\pi]$  present the colatitude and longitude.

The inner boundary velocity and tangential magnetic field, denoted by  $\mathbf{v}_s$ ,  $B_{\theta,s}$  and  $B_{\phi,s}$ , are defined the same as in Wang et al. (2025c,e), the pressure is set to  $p_s = 0.01 \text{ Pa}$ , and the inner boundary plasma density  $\rho_s$  is defined as a piecewise polynomial in the magnetic field strength  $|\mathbf{B}_s| = \sqrt{B_{r,s}^2 + B_{\theta,s}^2 + B_{\phi,s}^2}$ :

$$\rho_s(|\mathbf{B}_s|) = \begin{cases} \frac{\rho_{\text{ref1}} - \rho_{\text{ref}}}{B_{\text{ref1}}} \cdot |\mathbf{B}_s| + \rho_{\text{ref}}, & \text{if } |\mathbf{B}_s| \leq B_{\text{ref1}} \\ \frac{(\rho_{\text{ref2}} - \rho_{\text{ref1}}) \cdot (|\mathbf{B}_s| - B_{\text{ref1}})}{B_{\text{ref2}} - B_{\text{ref1}}} + \rho_{\text{ref1}}, & \text{if } B_{\text{ref1}} \leq |\mathbf{B}_s| < B_{\text{ref2}} \\ \frac{(\rho_{\text{ref3}} - \rho_{\text{ref2}}) \cdot (|\mathbf{B}_s| - B_{\text{ref2}})}{B_{\text{ref3}} - B_{\text{ref2}}} + \rho_{\text{ref2}}, & \text{if } B_{\text{ref2}} \leq |\mathbf{B}_s| \end{cases}, \quad (5)$$

where  $\rho_{\text{ref}} = 3.34 \times 10^{-13} \text{ kg m}^{-3}$  is the inner boundary density adopted in Wang et al. (2025e).  $\rho_{\text{ref1}} = 3.56 \times 10^{-13} \text{ kg m}^{-3}$ ,  $\rho_{\text{ref2}} = 16.94 \times 10^{-13} \text{ kg m}^{-3}$ , and  $\rho_{\text{ref3}} = 135.96 \times 10^{-13} \text{ kg m}^{-3}$  denote the plasma densities at 6 Mm above the photosphere derived from three surface-to-corona simulations performed with the *Bifrost* radiative MHD code (Gudiksen et al. 2011). These aim at spanning different QS typical configurations, from weakly magnetized QS conditions to network-like emergence episodes (Noraz et al. 2026), each configured with photospheric magnetic field of  $B_{\text{ref1}} = 21 \text{ G}$ ,  $B_{\text{ref2}} = 61 \text{ G}$ , and  $B_{\text{ref3}} = 89 \text{ G}$ , respectively.

Since the numerical stability of COCONUT in addressing low- $\beta$  issues has been substantially improved by Wang et al. (2025d), we remove the pressure PP treatment (Wang et al. 2025e) to minimise the influence of algorithmic uncertainties. Meanwhile, we retain the PP measure on density (Wang et al. 2025e) to prevent potential code failures in the challenging time-evolving solar-maximum CR simulations.

## 3. Numerical results

In this section, we present the simulation results. About 1300 hourly-updated GONG-zqs photospheric magnetograms<sup>2</sup> from CRs 2282 and 2283, spanning from 22:14 on March 12, 2024, to 11:14 on May 6, 2024, are used to drive the coronal evolutions. To achieve an appropriate balance between accuracy and computational efficiency in the time-evolving coronal simulations, we use a time step of 5 min. Three time-evolving simulations using different heating source terms and photospheric magnetogram

<sup>2</sup> <https://gong.nso.edu/data/magmap/QR/zqs/>

preprocessing methods, as indicated in Table 1, are compared to evaluate numerical uncertainties.

For case 1, the maximum magnetic field strength and the minimum plasma- $\beta$  in the low corona around active regions are typically about 17 G and  $9 \times 10^{-3}$ , respectively, and can occasionally reach values as high as 27 G and as low as  $3 \times 10^{-3}$ . For cases 2 and 3, the maximum magnetic field strength and the minimum plasma- $\beta$  are typically around 60 G and  $6 \times 10^{-4}$ , respectively, and can occasionally reach values as high as 99 G and as low as  $3 \times 10^{-4}$ . All simulations are performed using 720 parallel processes on the WICE cluster, which is part of the Tier-2 supercomputer at the Vlaams Supercomputer Centrum<sup>3</sup>. Under this configuration, the simulations run approximately 35-40 times faster than real-time evolutions.

### 3.1. Coronal evolutions under different numerical setups

In this subsection, we present the simulated coronal evolution in three cases and compare the results with observations to validate the model and assess the impact of numerical uncertainties on the simulated coronal structures.

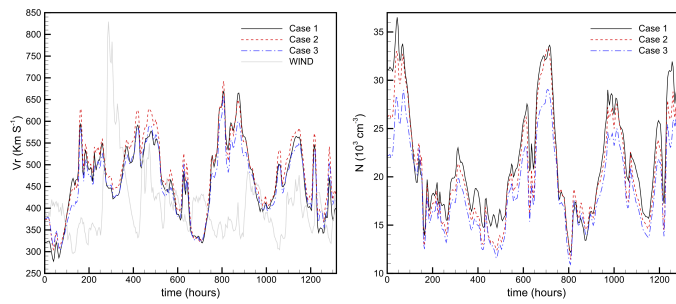


**Fig. 1.** Timing diagrams of the radial velocity  $V_r$  ( $\text{km s}^{-1}$ ; left) and proton number density ( $10^3 \text{ cm}^{-3}$ ; right) measured by a virtual satellite located at  $21.5 R_s$ . The virtual satellite is positioned at the same latitude as Earth but lags by  $60^\circ$  in longitude. The solid black, dashed red, and dashed-dot blue lines represent the time-evolving simulation results from Cases 1, 2, and 3, respectively, while the solid grey lines show the radial velocity (left) observed by the WIND spacecraft.

During these simulations, a virtual satellite is placed at  $21.5 R_s$ . It lags the Sun–Earth line by  $60^\circ$ , assuming that the solar wind takes approximately 100 hours to travel from 0.1 to 1 AU (Wang et al. 2025e,f). Fig. 1 shows that the simulated radial velocity in Case 2 is generally higher than in Cases 1 and 3, while the density in Case 1 is typically higher than in Cases 2 and 3, with the most pronounced differences occurring near the peaks. Although the overall time-evolving profiles of these variables are largely consistent across the three cases, the comparison between Cases 1 and 2 shows that the magnetogram over-filtered by the 10th-order PF solver leads to relatively higher plasma density and lower radial velocity, whereas the comparison between Cases 2 and 3 indicates that a minor modification in the radial distribution of the heating source term can reduce both the radial velocity and plasma density, with an effect that is more pronounced than that resulting from variations in magnetogram filtering. This underscores the need to explore more realistic heating mechanisms for coronal MHD simulations.

It is also noted that the simulated radial-velocity trough, centred around the 50th hour, occurs approximately 70 hours later than the observed one. The velocity peak and trough, centred

**Table 2.** Area-averaged radial velocity  $V_{r,\text{ave}}$  and proton number density  $N_{\text{ave}}$  in Fig. 2.

Case	$V_{r,\text{ave}}$ ( $\text{km s}^{-1}$ )	$N_{\text{ave}}$ ( $10^3 \text{ cm}^{-3}$ )
1	433.21	20.11
2	436.82	19.92
3	426.73	17.53

around the 300th and 800th hours, are mismatched in the simulations, with a trough and a peak. Meanwhile, the simulated radial velocity between the 450th and 650th hours is largely consistent with the observations, and the simulated troughs around the 1000th, 1200th, and 1250th hours closely match the observed ones. The oversimplified empirically defined heating source terms, the lack of accurate magnetic field observations in the polar regions, the exclusion of transient events such as CMEs from the simulations, and the neglect of the complex evolution of solar-wind structures in interplanetary space can all contribute to the discrepancies between simulations and *in situ* observations.

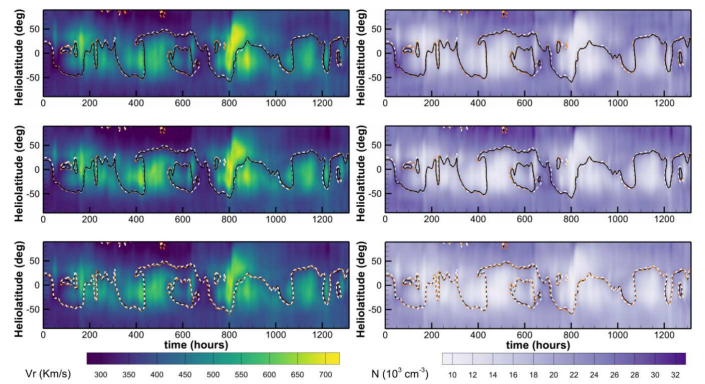


**Fig. 2.** Timing diagrams of the simulated radial velocity  $V_r$  ( $\text{km s}^{-1}$ ; left) and plasma number density ( $10^3 \text{ cm}^{-3}$ ; right) from Cases 1 (top), 2 (middle), and 3 (bottom) at 0.1 AU, evaluated along the latitudes intersected by longitude  $0^\circ$ , lagging the Sun–Earth line by  $60^\circ$  in longitude. The dashed white, dashed orange, and solid black lines denote the magnetic neutral lines (MNLs) derived from Cases 1, 2, and 3, respectively.

Fig. 2 further shows that the distributions of the magnetic neutral lines (MNLs) are highly consistent with the locations of high-density, low-speed flows. Additionally, the time-evolving latitudinal distributions of density and velocity at 0.1 AU are consistent across the three cases, with discrepancies primarily near abruptly reflecting MNLs. Furthermore, Table 2 lists the area-averaged radial velocity  $V_{r,\text{ave}}$  and proton number density  $N_{\text{ave}}$  evaluated on these panels shown in Fig. 2. These results demonstrate that the minor adjustments to the heating distribution introduced in this paper regulate the magnitudes of the simulated velocity and density at 0.1 AU more effectively than the truncation of high-order spherical harmonic components during magnetogram preprocessing, while all three cases preserve the overall tangential coronal structures.

Fig. 3 shows that the simulated polarised brightness (pB) images (Wang et al. 2025d) in Cases 1, 2, and 3 agree well with each other. Compared with the observations, the simulation at the 264th hour captures four bright structures, and the observed structure centred near  $30^\circ$  N on the east limb is shifted northward by approximately  $20^\circ$  in the simulation. In addition, the simulated bright structures near both polar regions are not present

<sup>3</sup> <https://www.vscentrum.be/>

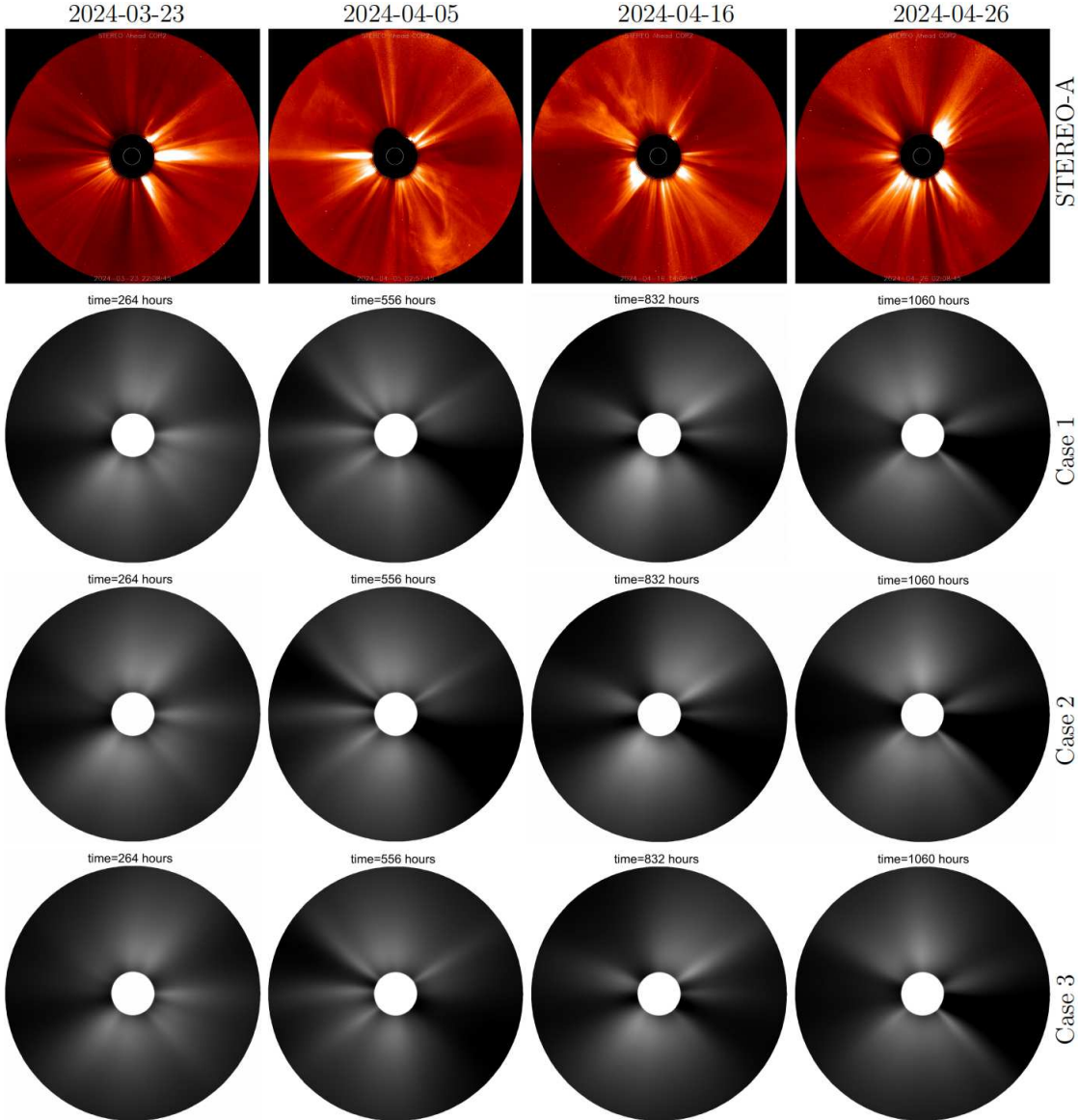


**Fig. 3.** White-light pB images observed by COR2/STEREO-A (first row) and synthesised from the coronal simulation results of Case 1 (second row), Case 2 (third row), and Case 3 (fourth row), respectively, spanning along heliocentric distances from 2.5 to  $15 R_s$  on meridional planes in the STEREO-A view. The orange lines indicate magnetic field lines on the selected meridional planes traced from identical seed points. The evolution of these simulated images during the simulated period is shown in online movie 1.

in the observations. At the 556th hour, the simulations reproduce the observed features at low and middle latitudes. Meanwhile, some bright structures still appear near the polar regions that are absent in the observations. At the 832nd hour, the observed bright structures around  $50^\circ$  S on both the west and east limbs merge into a wide bright feature covering the southern polar region. Meanwhile, the observed bright structure near the northern pole is rotated clockwise by approximately  $20^\circ$ , and the two simulated low-latitude bright structures agree well with the observations. At the 1060th hour, the high-latitude bright structure covering the southern pole is successfully reproduced. However, the bright structures along the equator on the east limb and near  $60^\circ$  on the west limb are absent in the simulations, whereas the observed bright structures near the northern pole and around  $50^\circ$  N in the east limb are basically reproduced in simulations. From these comparisons, it is evident that the pB images in the polar regions exhibit the largest discrepancies between simula-

tions and observations, indicating an urgent need to drive time-evolving coronal evolution during solar maximum using more realistic magnetograms and improved polar-region observations.

### 3.2. Evolution of open field region and open magnetic flux

In this subsection, we evaluate the evolution of open magnetic flux during CRs 2282 and 2283 at different heliocentric distances. Magnetic field lines are traced from  $150 \times 300$  uniformly distributed seed points on a spherical surface at  $10 R_s$  in both the sunward and the anti-sunward directions, and a field line is classified as open at  $r = r_{se}$  if it reaches both  $r_{se}$  and  $15 R_s$ . After determining the footpoints of the open magnetic field lines at  $r = r_{se}$ , we compute the distance between each sample point and the set of derived footpoints. A sample point is classified as belonging to an open-field region if the mini-

num distance is less than  $0.01\pi R_{\text{se}}$ . In this work, we adopt  $150 \times 300$  uniformly distributed sample points on the spherical surface at  $r = R_{\text{se}}$ . The unsigned open flux at  $R_{\text{se}}$  is calculated as

$$\Phi_{\text{open at } R_{\text{se}}} = \sum_{i=1}^{N^{\text{open at } R_s}} |B_{r,i}^{\text{open at } R_{\text{se}}}| \cdot S_i^{\text{open at } R_s} \text{ where } B_{r,i}^{\text{open at } R_{\text{se}}}$$

$S_i^{\text{open at } R_s}$  denote the radial magnetic field at the  $i$ th sample point within the open-field region and the discretised area associated with that point, respectively, and  $N^{\text{open at } R_s}$  denotes the number of the sample points belonging to open-field regions at  $R_{\text{se}}$ .

In Fig. 4, the top-left panel shows that the fluctuation frequency of the simulated radial magnetic field strength is basically consistent with the observations, whereas its magnitude is approximately only half of the observed value estimated by scaling the *in situ* observations at 1 AU by  $(0.1 \text{ AU}/1 \text{ AU})^2$ . The bottom-right panel shows that the simulated total unsigned magnetic flux at 0.1 AU is also approximately half of the averaged interplanetary magnetic flux derived from hourly averaged WIND satellite<sup>4</sup> (King & Papitashvili 2005) observations, consistent with the latitudinal invariance of the interplanetary magnetic field distribution. From the bottom-left panel of Fig. 4 and Table 3, it is also noticed that the open unsigned magnetic flux derived from the simulations at  $1.01 R_s$  in Cases 2 and 3 amounts to approximately 85% of the interplanetary magnetic flux  $\Phi_{\text{IAU}}^{\text{ave}}$ , and about 77% in Case 1. Here,  $\Phi_{\text{IAU}}^{\text{ave}} = 7.67 \times 10^{14} \text{ Wb}$  is derived from hourly averaged WIND *in situ* observations during CRs 2282 and 2283 and is comparable to the interplanetary open flux inferred from hourly averaged *in situ* measurements during CR 2101 reported by Linker et al. (2021). Considering that hourly averaged interplanetary magnetic field measurements tend to overestimate the open magnetic flux due to the commonly occurring inversions of the interplanetary magnetic field, and that the ratio between the open flux inferred from hourly averaged *in situ* observations and that derived from daily averaged data, which mitigate the effects of magnetic field inversions, is 137% (the corresponding ratio reported by Linker et al. (2021) is approximately 130%), we conclude that the simulated open magnetic flux evaluated in the low corona in all three cases is generally consistent with the interplanetary observations.

Additionally, the bottom-left panel shows that, in Cases 2 and 3, the open unsigned magnetic flux derived from the simulations decreases from 88% and 83% to 57% and 54% of the interplanetary magnetic flux  $\Phi_{\text{IAU}}^{\text{ave}}$  between  $1.01 R_s$  and  $3 R_s$ , and is further reduced by about 7% of  $\Phi_{\text{IAU}}^{\text{ave}}$  at 0.1 AU. The reduction in the simulated unsigned open magnetic flux with increasing heliocentric distance may be explained by the following factors. In the low corona, numerous small-scale closed magnetic structures are embedded within regions of open magnetic field. Some of these structures carry magnetic fields with polarity opposite to that of the surrounding open field, giving rise to many polarity inversion interfaces between open and closed fields. In grid cells that straddle these interfaces, adjacent open and closed magnetic fields of opposite polarity partially cancel during the volume-integration procedure of the finite-volume method, leading to an apparent reduction in the simulated unsigned open magnetic flux in the low corona. However, with increasing heliocentric distance, these small-scale closed-field structures gradually disappear, as shown in Figs. 5 and 6 and the top-right panel of Fig. 4. The fraction of open-field regions at  $3 R_s$  is approximately 2.6, 2.3, and 2.5 times that at  $1.01 R_s$  for Cases 1, 2, and 3, respectively. The ratio of open to total unsigned magnetic flux increases from about 40%, 40%, and 38% at  $1.01 R_s$  to approximately

97%, 96%, and 96% at  $3 R_s$  for Cases 1, 2, and 3, respectively. This indicates a pronounced decrease in closed-field structures that embedded in open-field regions with increasing heliocentric distance. Consequently, there are far fewer polarity inversion interfaces in the high corona, and the reduction of the simulated unsigned open magnetic flux becomes much slower.

It is also noticed that, although both the total and open unsigned magnetic fluxes at  $1.01 R_s$  in Case 1 are smaller than those in Case 2, they become nearly identical at  $3 R_s$  and 0.1 AU. Moreover, the ratio of open to total unsigned magnetic flux remains nearly the same for Cases 1 and 2 at both  $1.01 R_s$  and  $3 R_s$ . This indicates that the higher-order spherical harmonic components retained in Case 2 increase both the open and closed unsigned magnetic flux in the low corona, but do not affect the amount of open magnetic flux farther from the solar surface. In addition, the open unsigned magnetic flux in Case 2 is consistently larger than that in Case 3 at  $1.01 R_s$ ,  $3 R_s$ , and 0.1 AU, indicating that variation in heating source terms can effectively impact the evolution of the open unsigned magnetic flux.

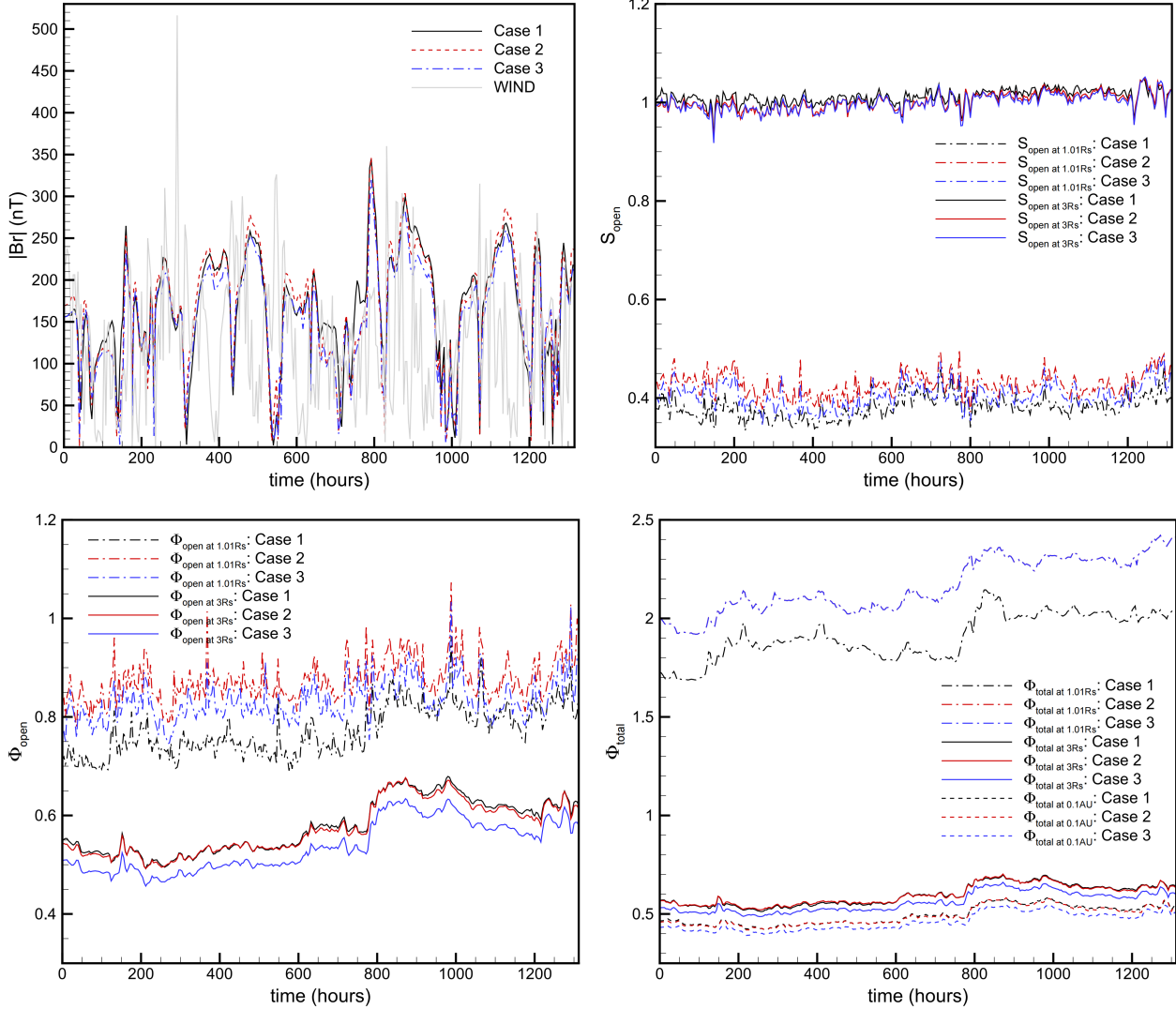
Fig. 5 illustrates the distributions of the radial magnetic field strength at  $1.01 R_s$  from Case 3, together with the corresponding open-field regions from Cases 1, 2, and 3 at three selected moments during the simulation period. It is observed that a dipolar structure near  $(\theta, \phi) = (20^\circ \text{ N}, 220^\circ)$  during the first 500 hours gradually shifts to  $(\theta, \phi) = (20^\circ \text{ N}, 220^\circ)$  in the subsequent evolution. Meanwhile, a dipolar structure near  $(\theta, \phi) = (10^\circ \text{ S}, 210^\circ)$  emerges at the 264th hour and persists throughout the subsequent evolution. At the 1316th hour, an additional dipolar structure appears near  $(\theta, \phi) = (20^\circ \text{ S}, 350^\circ)$ . Throughout the simulations, it is observed that in Cases 2 and 3, portions of both poles of the dipolar structures are always overlain by open-field regions that pass through their centres. Moreover, the north and south polar regions remain dominated by open-field regions, with only minor differences between them. The distributions of open-field regions in Cases 2 and 3 differ mainly in areas of weak magnetic field strength near the MNLs. It also indicates that the edges of the open-field regions in Case 1 fluctuate around those in Cases 2 and 3, with the most pronounced deviations occurring in both polar regions.

Fig. 6 shows the evolution of the radial magnetic field strength at  $3 R_s$  from Case 3, together with the corresponding open-field region boundaries at  $3 R_s$  derived from Cases 1, 2, and 3. It is observed that the maximum magnetic field strength decreases from approximately 70 G at  $1.01 R_s$  to around 0.13 G at  $3 R_s$ . Variations in dipolar structures observed at  $1.01 R_s$  are also reflected at  $3 R_s$ . For example, the enhancement of the magnetic field strength at the positive pole of the dipole near  $(\theta, \phi) = (10^\circ \text{ S}, 210^\circ)$  at  $1.01 R_s$  at the 832nd hour corresponds to a patch of the obviously increased magnetic field centred around  $(\theta, \phi) = (15^\circ \text{ S}, 170^\circ)$  at  $3 R_s$ . Although the fraction of the spherical surface occupied by open-field regions increases significantly from  $1.01 R_s$  to  $3 R_s$ , particularly for regions covering both the northern and southern poles, a considerable fraction of closed-field regions still persists at  $3 R_s$ . It is also noticed that the differences in the open-field region distributions between Cases 2 and 3 become less pronounced at  $3 R_s$  than at  $1.01 R_s$ .

## 4. Concluding remarks

Recently, a decomposed energy strategy that updates the decomposed energy consisting of internal and kinetic energy components at each time step, combined with an HLL Riemann solver that introduces an additional dissipation term in the energy equation, has been proposed and validated in Wang et al. (2025d).

<sup>4</sup> <https://cdaweb.gsfc.nasa.gov/index.html/>



**Fig. 4.** Timing diagrams of the radial magnetic field strength measured by the same virtual satellite as in Fig. 1, together with the WIND observations scaled by  $0.5 \times (1 \text{ AU}/0.1 \text{ AU})^2$  (nT; top left), as well as timing diagrams of the simulated areas of open-field regions ( $S_{\text{open}}$ ; top right) and the unsigned open magnetic flux ( $\Phi_{\text{open}}$ ; bottom left) at  $1.01 R_s$  and  $3 R_s$ , and the total unsigned magnetic flux ( $\Phi_{\text{total}}$ ; bottom right) across spherical surfaces at  $1.01 R_s$ ,  $3 R_s$ , and  $0.1 \text{ AU}$ . The magnetic fluxes  $\Phi_{\text{open}}$  and  $\Phi_{\text{total}}$  are normalized using the WIND *in situ* observations,  $\Phi_{1\text{AU}}^{\text{ave}} = |B_{r,1\text{AU}}|^{\text{ave}} \cdot 4\pi (1 \text{ AU})^2 = 7.67 \times 10^{14} \text{ Wb}$ , where  $|B_{r,1\text{AU}}|^{\text{ave}}$  denotes the average unsigned radial interplanetary magnetic field strength along the Sun-Earth direction, derived from hourly averaged WIND observations during the simulated period. The areas of the open-field regions at  $r = r_{\text{Se}}$  are normalized by  $S_{\text{open}}^{\text{ave}} \cdot (r_{\text{Se}}/3R_s)^2$ , where  $S_{\text{open}}^{\text{ave}} = 4.92 \times 10^{19} \text{ m}^2$  denotes the average open-field area at  $3 R_s$  in Case 3. The black, red, and blue curves correspond to results obtained from Cases 1, 2, and 3, respectively.

**Table 3.** Averaged total and open unsigned magnetic fluxes,  $\Phi_{\text{total,ave}}$  and  $\Phi_{\text{open,ave}}$ , normalized by the observed interplanetary magnetic flux, and the averaged open-field region area,  $S_{\text{open,ave}}$ , normalized by the average open-field area at  $3 R_s$  in Case 3 and scaled by  $(\frac{3R_s}{r_{\text{Se}}})^2$  with  $r_{\text{Se}} \in (1.01 R_s, 3 R_s)$ .

Case	$\Phi_{\text{total,ave}}$ at $1.01 R_s$ , $3 R_s$ & $0.1 \text{ AU}$	$\Phi_{\text{open,ave}}$ at $1.01 R_s$ & $3 R_s$	$S_{\text{open,ave}}$ at $1.01 R_s$ & $3 R_s$
1	1.910, 0.596 & 0.494	0.771 & 0.577	0.382 & 1.012
2	2.165, 0.597 & 0.491	0.875 & 0.573	0.427 & 1.002
3	2.165, 0.560 & 0.461	0.833 & 0.538	0.405 & 1.000

This approach significantly improves the numerical stability of the time-evolving MHD coronal model COCONUT (Wang et al. 2025c,e). The high efficiency inherent to implicit temporal integration, together with the improved numerical stability, makes the novel MHD coronal model COCONUT well suited for evaluating several uncertainties in solar-maximum coronal simula-

tions involving low- $\beta$  near active regions in the low corona. Meanwhile, it facilitates exploration of the “open flux problem” during solar maximum using time-evolving MHD coronal simulations without discarding much of the small-scale structure in the photospheric magnetograms, thereby providing a more re-

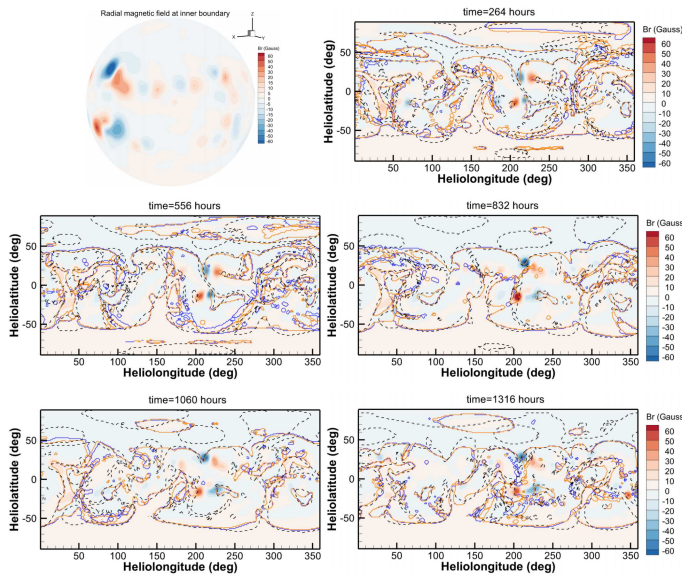


**Fig. 5.** Distributions of the radial magnetic field at  $1.01 R_s$  evaluated at the 264th, 556th, 832nd, 1060th, and 1316th hours for Case 3. The dashed black, solid orange, and solid blue lines overlaid on the magnetic-field contours denote the boundaries of open-field regions derived from Cases 1, 2, and 3, respectively. colour blueEvolution of the radial magnetic field at the inner boundary, as displayed in the top-left panel, during the simulated period is shown in online movie 2.

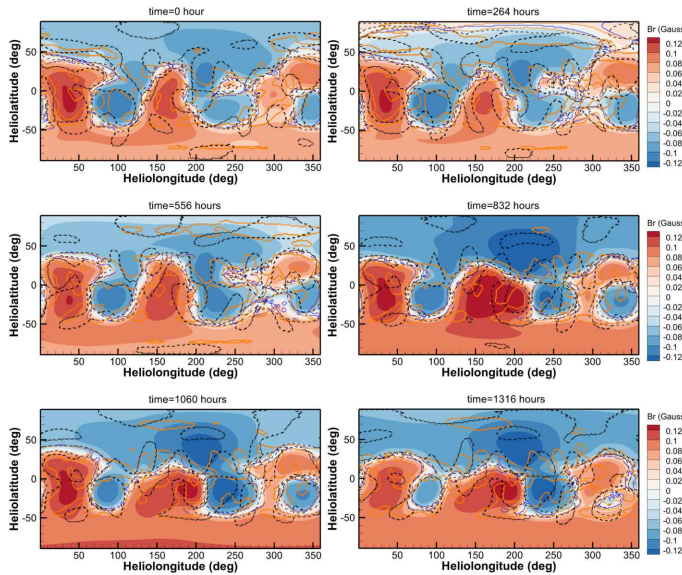


**Fig. 6.** Distributions of the radial magnetic field at  $3 R_s$  evaluated at the 0th, 264th, 556th, 832nd, 1060th, and 1316th hours for Case 3. The dashed black, solid orange, and solid blue lines overlaid on the magnetic-field contours denote the boundaries of open-field regions derived from Cases 1, 2, and 3, respectively.

alistic representation than commonly used quasi-steady simulations.

In this paper, we perform three time-evolving coronal simulations during CRs 2282 and 2283, driven by a sequence of hourly-updated photospheric magnetograms preprocessed with a 10th-order PF solver and a filtered 50th-order PF solver. The former removes many small-scale magnetic structures and re-

duces the magnetic field strength, thereby helping to avoid numerical stability issues in MHD modelling at the cost of reduced accuracy. In contrast, the latter preserves much more small-scale structure and is accompanied by low- $\beta$  challenges in MHD coronal simulations. In addition, we adjust the empirically defined heating source terms to assess the impact of empirically defined heating uncertainties, one of the most challenging issues in coronal modelling, on the simulated evolution of coronal structures, including the open magnetic flux at different heliocentric heights.

All these simulations reproduce reasonably high-density low-speed and low-density high-speed stream distributions. Additionally, the simulation results generally capture the observed white-light pB images and reflect the variations of solar wind structures inferred from interplanetary *in situ* observations. Further improvements, such as including physically based heating source terms like the wave turbulence-driven heating mechanism or more complex empirically defined volumetric heating terms that account for magnetic field topology, improving the spatio-temporal accuracy of magnetogram observations, especially in the polar regions, and incorporating transient events such as CMEs, may lead to better agreement between simulations and observations. To further improve the physical realism of the lower boundary, we implement non-uniform density boundary conditions based on parametrisations derived from local radiative MHD simulations performed with the *Bifrost* code, enabling more physically informed conditions at the base of the corona, which is key for magnetic-wind driving. This parametrisation should be regarded as a first proof of concept, and future work will focus on refining and extending it to further improve the realism of the lower boundary conditions.

The simulation results indicate that moderate adjustments to the empirically defined heating source term can effectively regulate the magnitude of the unsigned open magnetic flux, underscoring the need to adopt more realistic heating mechanisms in coronal MHD modelling. This paper also indicates that small-scale magnetic structures removed from magnetograms by a PF solver that neglects high-order spherical harmonics can reduce both the total and open unsigned magnetic fluxes. However, they have little impact on the amount of the simulated open unsigned flux at larger heliocentric distances, although the distribution of open-field regions is noticeably influenced. We also find that adopting the filtered high-order PF solver not only mitigates ringing artefacts in the magnetic field distribution caused by limited-order spherical harmonics (Tóth et al. 2011), but also reduces the irregularly distributed closed-field fragments scattered within the open-field regions in the low corona, as shown in Appendix A.

It is noticed that the simulated unsigned open magnetic flux evaluated near the solar surface in simulations driven by high-fidelity magnetograms preprocessed using the 50th-order filtered PF solver is comparable to the unsigned interplanetary open flux derived from WIND *in situ* observations. However, the simulated unsigned open magnetic flux decreases with increasing heliocentric distance, particularly in the low corona, where many small-scale closed-field structures exist and progressively disappear with height. This can be attributed to the fact that, in the low corona, many small-scale closed magnetic structures are embedded within the surrounding open field, with some field of the closed-field structure having a polarity opposite to that of the surrounding open field. Consequently, many polarity inversion interfaces arise between the open and closed fields, and magnetic fields of opposite polarity that come into direct contact are partially cancelled within a grid cell that passes through such

interfaces during the volume-integration procedure of the finite-volume method, leading to an obvious magnetic flux deficit. In contrast, the high corona is more potential, with open fields, and only large structures, such as CMEs, which are very transient, streamers, pseudo-streamers, and cavities, can provide closed magnetic fields. Additionally, many of these large-scale closed-field structures, such as those provided by streamers, separate open fields of opposite polarity, making it easier to resolve the open flux accurately. Therefore, the obvious reduction of polarity inversion interfaces in the high corona leads to a much slower decrease of the open unsigned flux with increasing heliocentric distance. This indicates that coronal simulations employing adaptive mesh refinement, with finer meshes near polarity inversion regions, are required to further reduce this magnetic flux deficit.

It is also noted that the simulated magnetic field strength at 0.1 AU, sampled by a virtual satellite placed at the same heliographic latitude as Earth, is approximately half of the hourly averaged WIND *in situ* observations at 1 AU scaled by  $(\frac{0.1 \text{ AU}}{1 \text{ AU}})^2$ . Consistently, the simulated unsigned magnetic flux at 0.1 AU is also about half of the unsigned flux inferred from the hourly averaged WIND interplanetary observations. This suggests that during solar maximum, although MNLs can undergo sharp deflections and even form isolated closed structures at 0.1 AU, even extending up to  $50^\circ$  in latitude, the latitudinal variation of the magnetic field distribution can still be used to derive the total unsigned interplanetary magnetic flux. In future work, we will further investigate the “open flux problem” by extending the quasi-realistic time-evolving MHD coronal simulations beyond 1 AU, enabling direct comparisons between simulation results and corresponding interplanetary *in situ* observations during solar maximum.

Additionally, it shows that the unsigned open flux fluctuates significantly during coronal evolution around solar maximum, with the maximum unsigned open flux at  $3 R_s$  being more than 1.4 times the minimum during CRs 2282 and 2283. This underscores the need to evaluate flux evolution during solar maximum using time-evolving coronal simulations rather than the commonly employed quasi-steady-state simulations. Recently, Downs et al. (2025) has also performed time-evolving coronal simulations around CR 2282 using another state-of-the-art MHD coronal model, the Magnetohydrodynamic Algorithm outside a Sphere (MAS; Lionello et al. 2023; Mason et al. 2023). As discussed in (Baratashvili et al. 2025), MAS employs more realistic synchronised magnetograms, in which the magnetic fields at different longitudes correspond to the same time, to drive coronal evolution. MAS also includes the transition region and adopts a more physical consistent wave–turbulence–driven heating mechanism. We will incorporate these more realistic settings into the time-evolving coronal model COCONUT, which employs the more efficient implicit temporal integration method and the decomposed energy strategy to address low- $\beta$  issues, in future work.

**Acknowledgements.** This project has received funding from the European Research Council Executive Agency (ERCEA) under the ERC-AdG agreement No. 101141362 (Open SESAME). These results were also obtained in the framework of the projects FA9550-18-1-0093 (AFOSR), C16/24/010 (C1 project Internal Funds KU Leuven), G0B5823N and G002523N (WEAVE) (FWO-Vlaanderen), and 4000145223 (SIDC Data Exploitation (SIDEX), ESA Prodex). This work is also supported by the BK21 FOUR program of the Graduate School, Kyung Hee University (GS-1-JO-NON-20242364). The resources and services used in this work were provided by the VSC (Flemish Supercomputer Centre), funded by the Research Foundation – Flanders (FWO) and the Flemish Government. This work utilises data obtained by the Global Oscillation Network Group (GONG) program, managed by the National Solar Observatory and operated by AURA, Inc., under a cooperative agreement with the National Science Foundation. The

data were acquired by instruments operated by the Big Bear Solar Observatory, High Altitude Observatory, Learmonth Solar Observatory, Udaipur Solar Observatory, Instituto de Astrofísica de Canarias, and Cerro Tololo Inter-American Observatory. The authors also acknowledge the use of the STEREO/SECCHI data produced by a consortium of the NRL (US), LMSAL (US), NASA/GSFC (US), RAL (UK), UBHAM (UK), MPS (Germany), CSL (Belgium), IOTA (France), and IAS (France), and use of NASA/GSFC’s Space Physics Data Facility’s OMNIWeb service.

## References

Arge, C., Luhmann, J., Odstrcil, D., Schrijver, C., & Li, Y. 2004, *J. Atmos. Sol-Terr. Phys.*, 66, 1295  
 Arge, C. N., Leisner, A., Antiochos, S. K., Wallace, S., & Henney, C. J. 2024, *ApJ*, 964, 115  
 Aslanyan, V., Pontin, D. I., Scott, R. B., et al. 2022, *ApJ*, 931, 96  
 Asvestari, E., Temmer, M., Caplan, R. M., et al. 2024, *ApJ*, 971, 45  
 Badman, Samuel T., Bale, Stuart D., Rouillard, Alexis P., et al. 2021, *A & A*, 650, A18  
 Bale, S. D., Goetz, K., Harvey, P. R., et al. 2016, *Space Sci. Rev.*, 204, 49  
 Balogh, A., Southwood, D. J., Forsyth, R. J., et al. 1995, *Science*, 268, 1007  
 Baratashvili, T., Brchnelova, M., Linan, L., Lani, A., & Poedts, S. 2024, *A & A*  
 Baratashvili, T., Wang, H. P., Sorokina, D., Lani, A., & Poedts, S. 2025, *A & A*  
 Brchnelova, M., Kužma, B., Zhang, F., Lani, A., & Poedts, S. 2023, *A & A*, 676, 905880205  
 Burlaga, L. F. 1984, *Space Sci. Rev.*, 39, 255  
 Caplan, R. M., Downs, C., Linker, J. A., & Mikic, Z. 2021, *ApJ*, 915, 44  
 Cranmer, S. R. 2002, in *COSPAR Colloquia Series*, Vol. 13, *Multi-wavelength Observations of Coronal Structure and Dynamics*, ed. P. C. Martens & D. P. Cauffman (Pergamon), 3–12  
 Downs, C., Linker, J. A., Caplan, R. M., et al. 2025, *Science*, 388, 1306  
 Downs, C., Roussev, I. I., van der Holst, B., et al. 2010, *ApJ*, 712, 1219  
 Erdős, G. & Balogh, A. 2012, *ApJ*, 753, 130  
 Erdős, G. & Balogh, A. 2014, *ApJ*, 781, 50  
 Feng, X. S., Li, C. X., Xiang, C. Q., et al. 2017, *ApJS*, 233, 10  
 Feng, X. S., Liu, X. J., Xiang, C. Q., Li, H. C., & Wei, F. S. 2019, *ApJ*, 871, 226  
 Feng, X. S., Lv, J. K., Xiang, C. Q., & Jiang, C. W. 2023, *Mon. Not. R. Astron. Soc.*, 519, 6297  
 Feng, X. S., Ma, X. P., & Xiang, C. Q. 2015, *J. Geophys. Res.: Space Phys.*, 120, 10,159  
 Feng, X. S., Wang, H. P., Xiang, C. Q., et al. 2021, *ApJS*, 257, 34  
 Feng, X. S., Xiang, C. Q., Zhong, D. K., & Fan, Q. L. 2005, *Chin. Sci. Bull.*, 50, 672–678  
 Feng, X. S., Yang, L. P., Xiang, C. Q., et al. 2010, *ApJ*, 723, 300  
 Fisk, L. A. 2005, *ApJ*, 626, 563  
 Fox, N. J., Velli, M. C., Bale, S. D., et al. 2016, *Space Sci. Rev.*, 204, 7  
 Fränz, M. & Harper, D. 2002, *Planet. Space Sci.*, 50, 217  
 Frost, A. M., Owens, M., Macneil, A., & Lockwood, M. 2022, *Sol. Phys.*, 297  
 Gudiksen, B. V., Carlsson, M., Hansteen, V. H., et al. 2011, *A & A*, 531, A154  
 Hayashi, K., Abbott, W. P., Cheung, M. C. M., & Fisher, G. H. 2021, *ApJS*, 254, 1  
 Hoeksema, J. T., Abbott, W. P., Bercik, D. J., et al. 2020, *ApJS*, 250, 28  
 Iijima, H. 2025, *ApJ*, 993, 130  
 Jardine, M., Donati, J.-F., Arzoumanian, D., & de Vidotto, A. 2010, *Proc. Int. Astron. Union*, 6, 242–248  
 Johnstone, C., Jardine, M., & Mackay, D. H. 2010, *Mon. Not. R. Astron. Soc.*, 404, 101  
 Kimpe, D., Lani, A., Quintino, T., Poedts, S., & Vandewalle, S. 2005, in *Proc. 12th European Parallel Virtual Machine and Message Passing Interface Conference*, ed. D. K. B. Di Martino & J. J. Dongarra (Sorrento: Springer), 520–527  
 King, J. H. & Papitashvili, N. E. 2005, *J. Geophys. Res.: Space Phys.*, 110, A02104  
 Kužma, B., Brchnelova, M., Perri, B., et al. 2023, *ApJ*, 942, 31  
 Lani, A., Quintino, T., Kimpe, D., et al. 2005, in *LNCS 3514*, Vol. 1, *Computational Science ICCS 2005*, ed. V. S. Sunderan, G. D. van Albada, P. M. A. Sloot, & J. J. Dongarra, Emory University (Atlanta, GA, USA: Springer), 281–286  
 Lani, A., Villedieu, N., Bensassi, K., et al. 2013, in *AIAA 2013-2589*, 21th AIAA CFD Conference, San Diego (CA)  
 Li, Y. C., Wang, H. P., Jeong, H.-J., et al. 2025, *ApJS*, 281, 23  
 Linan, L., Regnault, F., Perri, B., et al. 2023, *A & A*, 675, A101  
 Linker, J. A., Caplan, R. M., Downs, C., et al. 2017, *ApJ*, 848, 70  
 Linker, J. A., Heinemann, S. G., Temmer, M., et al. 2021, *ApJ*, 918, 21  
 Linker, J. A., Mikić, Z., Biesecker, D. A., et al. 1999, *J. Geophys. Res.: Space Phys.*, 104, 9809  
 Lionello, R., Downs, C., Mason, E. I., et al. 2023, *ApJ*, 959, 77

Liu, X. J., Feng, X. S., Zhang, M., & Zhao, J. M. 2023, *ApJS*, 265, 19

Lockwood, M. 2002, *J. Geophys. Res.: Space Phys.*, 107, SSH 1

Lockwood, M., Forsyth, R. B., Balogh, A., & McComas, D. J. 2004, *Ann. Geophys.*, 22, 1395

Lockwood, M., Owens, M., & Rouillard, A. P. 2009, *J. Geophys. Res.: Space Phys.*, 114

Mackay, D. H. & Upton, L. A. 2022, *The Astrophysical Journal*, 939, 9

Mason, E. I., Lionello, R., Downs, C., et al. 2023, *ApJL*, 959, L4

McClarren, R. G. & Hauck, C. D. 2010, *J. Comput. Phys.*, 229, 5597

McComas, D. J., Bame, S. J., Barker, P., et al. 1998, *Space Sci. Rev.*, 86, 1572

Mikić, Z., Downs, C., Linker, J. A., et al. 2018, *Nature Astronomy*, 2, 913

Milić, I., Centeno, R., Sun, X., Rempel, M., & de la Cruz Rodríguez, J. 2024, *A & A*, 683

Mok, Y., Mikić, Z., Lionello, R., & Linker, J. A. 2005, *ApJ*, 621, 1098

Murteira, J., Brchnelova, M., Lani, A., & Poedts, S. 2025, *RAS Tech. Instrum.*, 4, rza030

Nakamizo, A., Tanaka, T., Kubo, Y., et al. 2009, *J. Geophys. Res.: Space Phys.*, 114

Noraz, Q., Carlsson, M., & Aulanier, G. 2026, *Astronomy & Astrophysics*, 705, A86

Owens, M. J., Arge, C. N., Crooker, N. U., Schwadron, N. A., & Horbury, T. S. 2008, *J. Geophys. Res.: Space Phys.*, 113

Owens, M. J., Lockwood, M., Riley, P., & Linker, J. 2017, *J. Geophys. Res.: Space Phys.*, 122, 10,980

Parenti, S., Réville, V., Brun, A. S., et al. 2022, *ApJ*, 929, 75

Perri, B., Brun, A. S., Réville, V., & Strugarek, A. 2018, *J. Plasma Phys.*, 84

Perri, B., Kužma, B., Brchnelova, M., et al. 2023, *ApJ*, 943, 124

Perri, B., Leitner, P., Brchnelova, M., et al. 2022, *ApJ*, 936, 19

Réville, V. & Brun, A. S. 2017, *ApJ*, 850, 45

Riley, P., Linker, J., Mikić, Z., et al. 2019, *ApJ*, 884, 18

Riley, P., Lionello, R., Caplan, R. M., et al. 2021, *A & A*, 650

Schrijver, C. J. & De Rosa, M. L. 2003, *Sol. Phys.*, 212, 165

Sinjan, J., Solanki, S. K., Hirzberger, J., Riethmüller, T. L., & Przybylski, D. 2024, *Astronomy & Astrophysics*, 690, A341

Sinjan, J., Solanki, S. K., Hirzberger, J., Riethmüller, T. L., & Przybylski, D. 2024, *A & A*, 690

Smith, C., L'Heureux, J., Ness, N., et al. 1998, *Space Sci. Rev.*, 86, 613

Smith, E. J. 2011, *J. Geophys. Res.: Space Phys.*, 116

Smith, E. J. & Balogh, A. 1995, *GRL*, 22, 3317

Tóth, G., van der Holst, B., & Huang, Z. 2011, *ApJ*, 732, 102

Ulrich, R. K., Bertello, L., Boyden, J. E., & Webster, L. 2009, *Sol. Phys.*, 255, 53

Upton, L. & Hathaway, D. H. 2014, *ApJ*, 780, 5

Wallace, S., Arge, C. N., Pattichis, M., Hock-Mysliwiec, R. A., & Henney, C. J. 2019, *Sol. Phys.*, 294

Wang, H. P., Guo, J. H., Poedts, S., et al. 2025a, *ApJS*, 281, 43

Wang, H. P., Guo, J. H., Yang, L. P., et al. 2025b, *A & A*, 10

Wang, H. P., Poedts, S., Lani, A., et al. 2025c, *A & A*, 694

Wang, H. P., Poedts, S., Lani, A., et al. 2025d [[arXiv:2508.20423](https://arxiv.org/abs/2508.20423)]

Wang, H. P., Poedts, S., Lani, A., et al. 2025e, *A & A*, 702, A37

Wang, H. P., Xiang, C. Q., Liu, X. J., Lv, J. K., & Shen, F. 2022a, *ApJ*, 935, 46

Wang, H. P., Yang, L. P., Poedts, S., et al. 2025f, *ApJS*, 278, 59

Wang, H. P., Zhao, J. M., Lv, J. K., & Liu, X. J. 2022b, *Chin. J. Geophys.*, 65, 2779

Wang, Y., Feng, X. S., & Xiang, C. Q. 2019, *Comput. Fluids*, 179, 67

Wang, Y.-M. & Sheeley, Jr., N. R. 1990, *ApJ*, 355, 726

Wang, Y. M., Ulrich, R. K., & Harvey, J. W. 2022, *ApJ*, 926, 113

Wenzel, K.-P., Marsden, R. G., Page, D. E., & Smith, E. J. 1992, *Astron. Astrophys. Suppl. Ser.*, 92, 207

Yang, L. P., Feng, X. S., Xiang, C. Q., et al. 2012, *J. Geophys. Res.: Space Phys.*, 117

Yeates, A. R., Mackay, D. H., van Ballegooijen, A. A., & Constable, J. A. 2010, *J. Geophys. Res.: Space Phys.*, 115

Yoshida, M., Shimizu, T., & Toriumi, S. 2023, *ApJ*, 950, 156

## Appendix A: Effects of filtered versus unfiltered PF Solver preprocessing on initial magnetograms

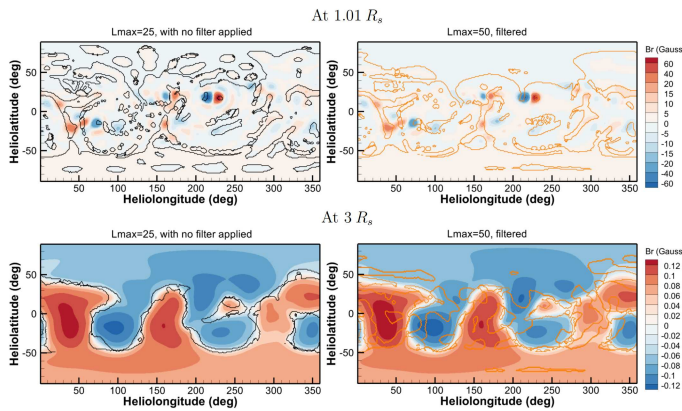


**Fig. A.1.** Distributions of the radial magnetic field at  $1.01 R_s$  (top) and  $3 R_s$  (bottom) preprocessed using the 25th-order PF solver (left) and the 50th-order filtered PF solver as described in Eq. 4 (right). These results correspond to the 0th hour of the simulated period. The solid lines overlaid on the magnetic-field contours indicate the boundaries of open-field regions derived from the corresponding coronal simulation results.

Fig. A.1 shows the distributions of the radial magnetic field at  $1.01 R_s$  and  $3 R_s$ , preprocessed using a 25th-order PF solver without filtering the spherical harmonic functions (left, Case 4) and a 50th-order PF solver with filtered spherical harmonic functions (right, Case 3), together with the corresponding open-field regions. The ring-like magnetic field structures evident in the left-top panel disappear in the right-top panel. The irregularly distributed closed-field patches scattered within the polar open-field regions are significantly reduced in the right-top panel. Additionally, the closed-field region at  $3 R_s$  shown in the bottom-left panel is largely aligned with the MNLs, whereas in the bottom-right panel, many parts of the closed-field region deviate from the MNLs. These images are derived from the simulated results at the 0th hour. The open magnetic flux, normalised in the same way as in Fig. 4, is 0.939 and 0.835 at  $1.01 R_s$ , 0.531 and 0.538 at  $3 R_s$ , and 0.453 and 0.458 at 0.1 AU, for Cases 4 and 3, respectively. Correspondingly, the ratios of open to total unsigned flux are 0.379 and 0.419 at  $1.01 R_s$ , and 0.962 and 0.964 at  $3 R_s$ , for Cases 4 and 3, respectively. These results further demonstrate that the spherical harmonic preprocessing of the magnetograms, which removes several small-scale magnetic structures, has little impact on the amount of simulated open unsigned flux at larger heliocentric distances, although it does influence the distribution of open-field regions and the amount of open unsigned flux in the low corona.